RSC Advances

PAPER

View Article Online
View Journal | View Issue

Cite this: *RSC Adv.*, 2020, **10**, 29961

Phyto-inspired and scalable approach for the synthesis of PdO–2Mn_2O_3: a nano-material for application in water splitting electro-catalysis†

Taghazal Zahra,[a] Khuram Shahzad Ahmad, *[a] Andrew Guy Thomas,[b] Camila Zequine,[c] Ram K. Gupta,[c] Mohammad Azad Malik[b] and Manzar Sohail[d]

A modified co-precipitation method has been used for the synthesis of a PdO–2Mn_2O_3 nanocomposite as an efficient electrode material for the electro-catalytic oxygen evolution (OER) and hydrogen evolution reaction (HER). Palladium acetate and manganese acetate in molar ratio 1 : 4 were dissolved in water, and 10 ml of an aqueous solution of phyto-compounds was slowly added until completion of precipitation. The filtered and dried precipitates were then calcined at 450 °C to obtain a blackish brown colored mixture of PdO–2Mn_2O_3 nanocomposite. These particles were analyzed by ultra violet visible spectrophotometry (UV-vis), infrared spectroscopy (FTIR), powder X-ray diffractometry (XRD), scanning electron microscopy (FE-SEM), energy dispersive X-ray spectroscopy (EDX) and X-ray photoelectron spectroscopy (XPS) for crystallinity, optical properties, and compositional and morphological makeup. Using Tauc's plot, the direct band gap (3.18 eV) was calculated from the absorption spectra. The average crystallite sizes, as calculated from the XRD, were found to be 15 and 14.55 nm for PdO and Mn_2O_3, respectively. A slurry of the phyto-fabricated PdO–2Mn_2O_3 powder was deposited on Ni-foam and tested for electro-catalytic water splitting studies in 1 M KOH solution. The electrode showed excellent OER and HER performance with low over-potential (0.35 V and 121 mV) and Tafel slopes of 115 mV dec^{-1} and 219 mV dec^{-1}, respectively. The outcomes obtained from this study provide a direction for the fabrication of a cost-effective mixed metal oxide based electro-catalyst *via* an environmentally benign synthesis approach for the generation of clean energy.

Received 23rd May 2020
Accepted 11th July 2020

DOI: 10.1039/d0ra04571c

rsc.li/rsc-advances

Introduction

The world is facing energy crisis because of the threatening consequences of global warming; thus clean energy sources are needed at the present time in order to lessen the burden on diminishing energy reservoirs.[1] The water splitting (WS) process is considered to be a cleaner energy generation process, which is the most addressed topic among researchers, attaining its thrust mainly due to the production of hydrogen and oxygen.[2,3] WS can be categorized as photo-electrochemical water splitting and electrochemical water splitting, which share many commonalities in their processes, but their difference lies in their energy sources, as PEC water splitting utilizes abundant solar energy while electrochemical water splitting harnesses electrical energy to produce hydrogen.[4] In water splitting the absorbed photons on the surface of electrodes results in the generation of electrons and holes which are used in hydrogen and oxygen evolution respectively. The water oxidation reaction is normally favorable in an alkaline medium because in an alkaline medium, even cheap materials can be used as coherent electrodes,[5,6] reducing corrosion and bidding for a long lifetime for the anode.[7] Sluggish kinetics of OER at the anode results in a large-over potential that leans towards low efficiency.[3] Henceforward the concern of researchers is to reduce the over-potential by using economically viable materials. Currently noble metals such as ruthenium oxide (RuO_2), iridium oxide (IrO_2), and Pt-based materials are considered as benchmarks for HER and OER reactions because of their efficient electro-catalytic activity.[8–12] Nonetheless, their long-term applicability on a large scale is really obstructed due to their high cost and scarcity. Therefore it is desirable to explore bi-functional electrode materials which have low cost, high abundance and excellent electro-catalytic efficiency with large-scale applicability towards OER and HER. Generally, transition metals or metal oxides: manganese oxides (MnOx),[13] ruthenium oxide (RuO_2),[14] nickel oxide (NiO),[15] palladium/palladium oxide[19–21] and cobalt oxides (CoOx),[16] are regarded as efficient electrode materials for redox-type applications. In PEC water splitting the absorbed photons on the surface of

[a]*Department of Environmental Sciences, Fatima Jinnah Women University, The Mall, Rawalpindi, Pakistan. E-mail: chemist.phd33@yahoo.com; dr.k.s.ahmad@fjwu.edu.pk*
[b]*Department of Materials, Photon Science Institute and Sir Henry Royce Institute, Alan Turing Building, The University of Manchester, Oxford Road, Manchester M13 9PL, UK*
[c]*Department of Chemistry, Pittsburg State University, 1701 South Broadway Street, Pittsburg, KS 66762, USA*
[d]*School of Natural Sciences, National University of Sciences and Technology (NUST), Islamabad, Pakistan*

† Electronic supplementary information (ESI) available. See DOI: 10.1039/d0ra04571c

the photoelectrodes result in the generation of electrons and holes which are used in hydrogen and oxygen evolution, respectively.[5,100,101] Since 1972 various metal oxides,[6,7] nitrides[8] and other composites with different bandgaps have been investigated as photoelectrodes for enhanced hydrogen and oxygen evolution.

Manganese based nanoparticles have gained huge attention and have been largely examined for electro-catalytic redox-type studies, mainly because of their low cost and high catalytic efficiency for different redox reactions.[17,18] However, the considerable electro-catalytic efficiency of Mn_2O_3 is less than those of RuO_2 or IrO_2 due to its low conductivity and high over-potential; however, its performance could be enhanced when mixed with other less expensive noble metal oxides. Palladium oxide is a relatively less expensive metal oxide than RuO_2 or IrO_2 and is considered to provide efficient electrochemical properties. Previously it has been studied that transition metal mixed oxides (M/MOx) are electro-catalytically more efficient than single metal oxides[19–22] and they have been synthesized previously by physical and chemical synthesis approaches. However, chemical synthesis methods based on chemical reducing agents have been a major concern because of their high cost, toxicity and non-biodegradable stabilizing agents posing a serious danger to the environment, *e.g.* $NaBH_4$ and $LiAlH_4$.[23–25] To deal with these shortcomings, successive phyto-synthetic routes have been investigated and reported,[26,27] as this synthesis approach has advantages over chemical methods in term of sustainability and viability.[28–30,38] Therefore in the present investigation bio-inspired palladium oxide has been combined with manganese oxide, considered as an electro-active material with prominent electro-catalytic performance.[31–33] The biogenic synthesis approach has been investigated as a facile, greener method using natural reducing agents to replace toxic chemical methods. By modifying a simple co-precipitation method,[40] *Olea ferruginea* Royle leaf extract (OFRLE) has been used as an organic template reducing agent instead of any chemical agent to fabricate an eco-friendly and cost-effective PdO–$2Mn_2O_3$ electro-catalyst. Previous phyto-chemical studies explored the selected plant having efficient bioactive compounds[34,35] (*e.g.*, benzenemethanol, propanedioic acid, and malonic acid) which have been used as chemical reducing and capping agents.[36,37] The phytocompounds induced C, O and N containing species which enhance the growth of particles in the synthesis process as well as affecting the catalytic efficiency of nanoparticles. Furthermore, the selected plant has been used for the first time for the synthesis of a mixed metal oxide (PdO–$2Mn_2O_3$). Thus the focus of the present study is to synthesize a cheap and environmentally benign mixed metal oxide nanomaterial using leaf extracts of the *Olea ferruginea* Royle (OFR) plant. The synthesized material was decorated on Ni-foam to study its electrochemical behavior towards water oxidation. The unique combination of PdO–$2Mn_2O_3$ exhibits prominent electro-catalytic performance for both OER and HER.

Materials and methods

Palladium(II)acetate [$Pd(CH_3CO_2)_2$], manganese acetate tetrahydrate [$Mn(CH_3CO_2)_2 \cdot 4H_2O$], and ethanol were purchased from Merck Chemicals Ltd. Acetylene black, polyvinylidene difluoride (PVDF) and *N*-methyl pyrrolidinone (NMP) were procured from Sigma-Aldrich and were used without further purification. Phytochemical extracts of *O. ferruginea* Royle (OFR) plant leaves were used as reducing cum stabilizing agents in the synthesis of PdO–$2Mn_2O_3$ and were sampled from the local village of Azad Jammu Kashmir, Pakistan.

Fresh leaves of *Olea ferruginea* Royle (OFR) were washed twice to remove dust and environmental particulates and placed in the shade for drying. After that the leaves were oven dried at 100 °C to remove all the moisture completely, they were ground to a fine powder with the help of a mortar and pestle and stored in air-tight labeled polythene bags to avoid moisture contamination. To prepare the leaf extract, 2 g of OFR leaf powder was taken and heated in 100 ml of distilled water at 50 °C for 30 min. After that, the obtained dark green solution was filtered using Whatman filter paper no. 1 (25 μm pore size). The prepared extract was stored at 4 °C for use as a reducing and stabilizing agent in the synthesis.

0.5 g (2 mM) of $Pd(CH_3CO_2)_2$ and 1.96 g (8 mM) of $Mn(CH_3CO_2)_2 \cdot 4H_2O$ were dissolved in a 500 ml beaker containing 250 ml of distilled water. 10 ml of the previously extracted OFR leaf extract was slowly added to the solution of metal acetates under stirring at 80 °C. An aliquot portion of the reaction mixture was taken and tested for complete precipitation. On completion of the precipitation process, the precipitates were coagulated, centrifuged for 10 min at 6000 rpm and rinsed twice with deionized water and finally with ethanol. The obtained precipitates were dried in a hot-air oven at 95 °C and then annealed in a muffle furnace at 450 °C for removal of any organic residuals the mechanism of synthesis of PdO–$2Mn_2O_3$ has been presented in Fig. 1.

PdO–$2Mn_2O_3$ nanoparticles were characterized by UV-vis spectroscopy: 1602, Biomedical Services, Spain, FTIR: 8400, Shimadzu, Japan, and GC-MS to identify the organic compounds acting as capping agents. The crystalline phase of PdO–$2Mn_2O_3$ was examined by p-XRD: Bruker Advanced X-ray Solutions D9. X-ray photoelectron spectroscopic (XPS) data were collected using a Kratos Axis Ultra spectrometer (monochromated Al Kα X-ray source, $h\nu$ = 1486.6 eV) to determine the surface chemistry. The synthesized material was analyzed by

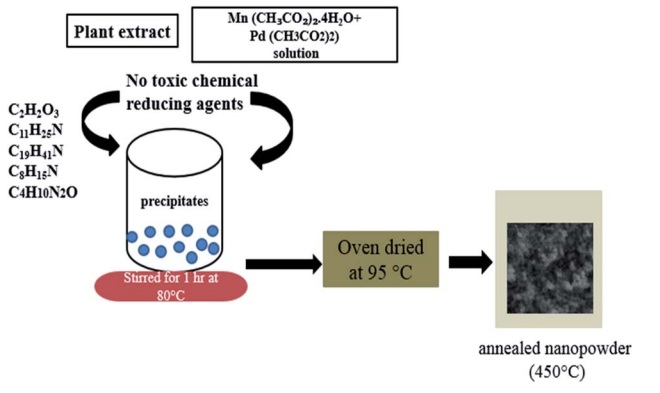

Fig. 1 Schematic representation of mechanism of synthesis of PdO–$2Mn_2O_3$.

energy dispersive X-ray spectroscopy (EDX) to confirm its purity and the bulk elemental composition. The structure and morphology were observed using Quanta-250 FEG scanning electron microscopy (FE-SEM) and transmission electron microscopy (TEM).

Fabrication and electrochemical study of prepared electrode

The fabrication of the prepared PdO–2Mn_2O_3 on Ni-foam as a working electrode was done by mixing 80 wt% of the synthesized NPs, 10 wt% of acetylene black, and 10 wt% of polyvinylidene difluoride in the presence of *N*-methyl pyrrolidinone (NMP). After homogeneous mixing, the slurry was deposited on Ni-foam and dried at 60 °C under vacuum for 12 hours. The average mass loading of electro-catalyst on Ni-foam was 2 mg cm^{-2}.

The catalytic activity of the synthesized material was electrochemically studied using a VersaSTAT 4-500 electrochemical workstation (Princeton Applied Research, USA) in the standard electrode configuration. A graphite rod, saturated calomel electrode (SCE), and synthesized palladium manganese bio-synthesized nanoparticles (PMBSNPs) on Ni-foam were used as counter, reference and working electrodes, respectively in 1 M KOH electrolyte solution. Electro-catalytic testing, including linear sweep voltammetry (LSV) and electrochemical impedance spectroscopy (EIS), were performed. LSV was performed at a rate of 1 mV s^{-1} for both OER and HER. Using the Nernst equation (eqn (1)) the potential was converted to RHE.[42] All EIS measurements were conducted in an applied 10 mV of AC amplitude with a frequency range of 0.05 Hz to 10 kHz. Over-potential (η) was calculated with eqn (2). To achieve a current density of 10 mA cm^{-2}:

$$E_{RHE} = E_{SCE} + 0.059\ pH + 0.1976 \quad (1)$$

$$\eta = E_{RHE} - 1.23\ V \quad (2)$$

Results and discussion

The phytochemical analysis and all the relevant detail have been given in Fig. S1, Tables S1 and S2.† The UV-vis analysis was performed with an OFR aqueous extract in the quartz cell and scanned in the wavelength range of 200 to 800 nm. The characteristic peaks of phytocompounds were observed in the ultra violet and visible region, as delineated in Fig. S2.† Aromatic conjugated fitting of the phenolic compounds assisted the UV-visible detectors to allocate phenolic components in the UV-visible spectral region. In Fig. S2(b)† the absorbance band at 271.01 nm corresponds to phenol corresponding to benzene ring-A conjugation. While the absorbances at 327 nm and 400 nm are consistent with flavonoids having conjugation of rings B and C. In addition, it is reported that absorption features between 300 to 330 nm are indicative of flavones and flavonols in the plant extract.[43]

The dried powder of the OFR leaf was subjected to FTIR spanning 400–4000 cm^{-1} to determine the phytocompounds of the selected plant. Table S2† exhibits the peaks with respective bond and functional group, which particularly identifies the

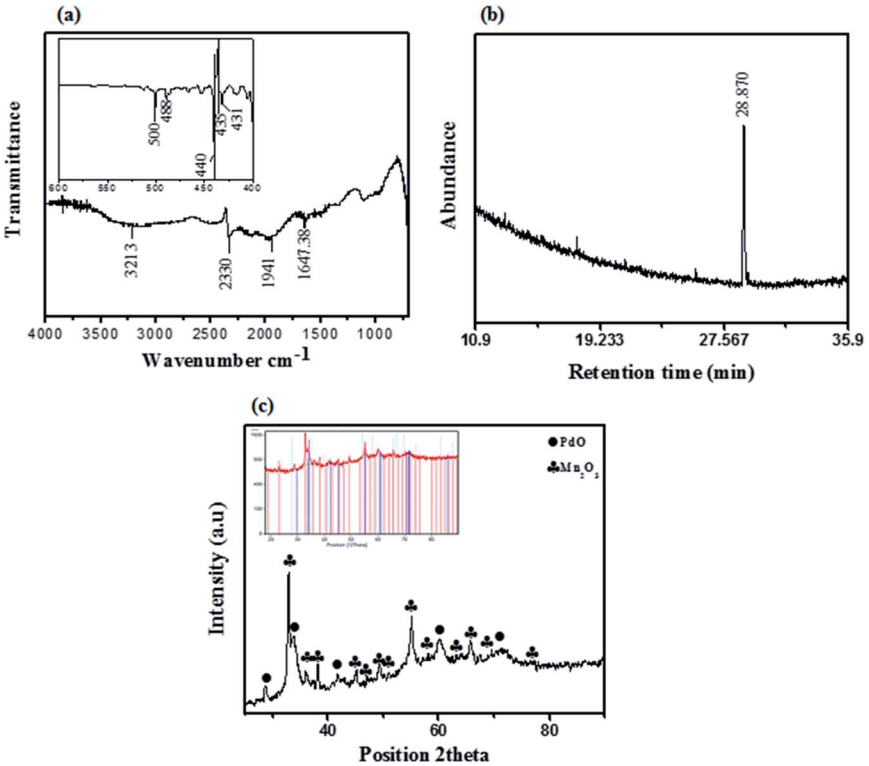

Fig. 2 (a) FTIR spectrum, (b) GCMS chromatogram and (c) X-ray diffractogram of synthesized PdO–2Mn_2O_3.

aliphatic amines and alkenes. The frequency range from 3400.62 cm^{-1} to 2922.25 cm^{-1} represents the O–H stretching vibration & –C=C– stretching, suggesting the presence of alcohols and phenols; alkanes and alkenes, respectively. The frequencies ranging between 1600 and 1100 suggest the presence of nitro-compounds; aromatic amines; alcohols, carboxylic acids, esters, and ethers. At frequencies of 1030.02 cm^{-1} and 875.71 cm^{-1}, C–N stretching and =C–H bending were observed, which refer to aliphatic amines and alkenes. A very minor vibration at 798.56 cm^{-1} was noticed because of =C–H bending and C–Cl stretching. The results from GC-MS analysis of the methanolic extract of the OFR extract identified various compounds at respective retention times. Bioactive compounds identified in OFR are benzenemethanol, cathinone, 3-azabicyclo nonane, propanedioic acid, and 1-cyclohexylethylamine. Consistent with the FTIR results, GCMS illustrates prominently the NH-bond containing compounds which are amino acids and amines with the highest weight% of cathinone. Cathinone is the monoamine alkaloid with a ketone group. After cathinone the highest weight% are of 1-cyclohexylethylamine, benzenemethanol and propanedioic acid, which represent the presence of phenols, flavonoids and amine groups, as proposed by spectroscopic analysis.

The synthesized PdO–2Mn_2O_3 nano-powder was scanned on FTIR and strong vibrations were observed below 500 cm^{-1} referring to the M–O (metal–oxygen) bond. O–H stretching appears as a broad band extending from 3200 cm^{-1} corresponding to aromatic groups (Fig. 2(a)). Some minor vibrations were observed at 3200 cm^{-1}, 2300 cm^{-1} and 1940 cm^{-1}, which do not correspond to any functional group, but are characteristic of a lot of hydrated compounds or adsorbed water on the surface of the pallets.[30,44,47] Vibration was observed, as shown in the inset of Fig. 2(a) at 500 cm^{-1}, 488 cm^{-1}, 400 cm^{-1}, 435 cm^{-1} and 431 cm^{-1}, representing the characteristics of metal oxide stretching.[45,46] As a consequence of the biological reduction mechanism, the proficient peak decreases at 3400 cm^{-1}, 1600 cm^{-1} and 1100 cm^{-1} confirmed the major reduction performance of phenols and proteins in comparison with the plant extract spectra (S1†). In the same way, the minor decrease in peaks between 1400 cm^{-1} and 1200 cm^{-1} demonstrated that carboxylic acids and esters are playing a less significant role in reduction activity. The peaks appearing in the range 2300 cm^{-1} indicated the generation of some species of alkanes during the process of reduction.[47] There are abundant phytocompounds, including benzaldehydes, phenols (catechin derivatives), benzoic acid derivatives (gallic acid, dihydro-*p*-coumaric acid derivative), esters and flavonoids in the leaf extract, which could be responsible for the functionalization of metal salts.[48,49]

Furthermore, with GC-MS the phytocompound as a stabilizing agent was identified in the methanolic suspension of PdO–2Mn_2O_3 nanoparticles. In Fig. 2(b) the chromatogram exhibits a sharp peak at 28.870 retention time, referring to decanoic acid according to the GC-MS profiling of the NIST library, which is an antioxidant present in medicinal plants.[50] Therefore GCMS endorsed the functionalization of PdO–2Mn_2O_3 by phytocompounds of OFR.

The purity and crystallinity of the as-synthesized material were examined by X-ray diffraction (XRD). The powder X-ray diffraction pattern of PdO–Mn_2O_3 oxide is shown in Fig. 2(c). Low and broad diffraction peaks can be seen which are due to the small size and incomplete inner structure of the particles. The relative peak intensities and position of palladium (PdO) and manganese oxide (Mn_2O_3) at diffraction peaks are in close agreement with JCPDS cards no. 00-006-0515 and 00-031-0825, respectively. PdO exhibits a tetragonal crystal system with cell parameters of $a = b = 3.0$, $c = 5.3$ Å and introduces characteristic peaks denoted by (●) at $2\theta = 33.87°$, 41.92°, 60.19° and 71.46° with their corresponding Miller indices (101), (110), (103)

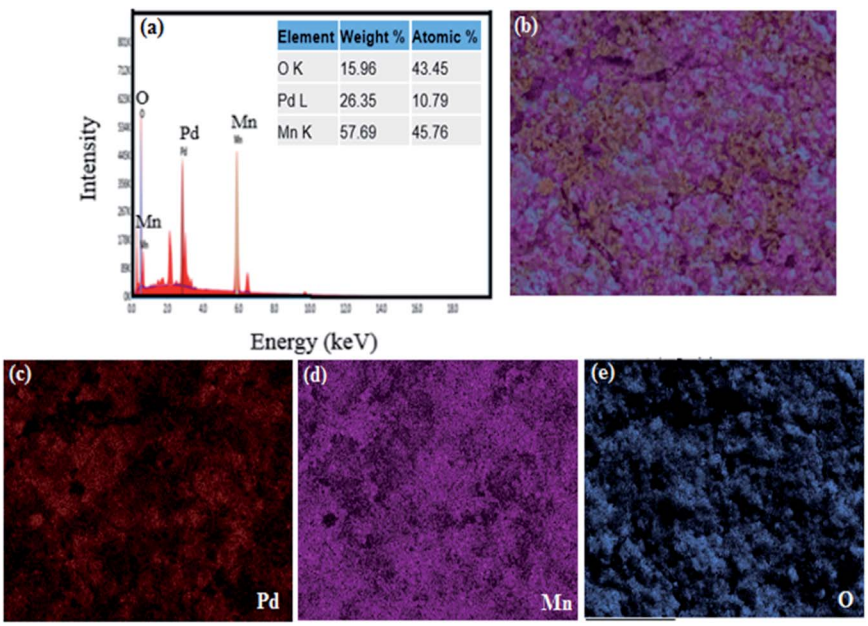

Fig. 3 (a) Elemental analysis of phyto-fabricated PdO–2Mn_2O_3 and (b)–(e) elemental mapping images of individual O, Mn, and Pd.

and (211). Mn_2O_3 exhibits a cubic crystal system with cell parameters of $a = b = c = 9.4$ Å. Diffraction peaks indicated by (♣) at 2θ values of 32.90°, 38.2°, 45.06°, 49.35°and 55.15° are associated with (222), (400), (332), (431) and (440), respectively, in a close match with the literature values.[76]

The average crystallite size of the most prominent peaks was determined by diffraction line broadening using the Scherer equation $D = (0.94\lambda)/(\beta \cos \theta)$, where θ is the diffraction angle, wavelength is represented by λ (1.542 Å) (Cu-Kα), and the FWHM of the diffraction line is represented by β. The estimated crystallite size for PdO was 15.44 nm and 14.55 nm for Mn_2O_3. Through elemental analysis (EDX) the purity and uniform composition of the nanoparticles were confirmed as described earlier by XPS and further confirmed by elemental mapping (Fig. 3(b)–(e)). The EDX spectrum is shown in Fig. 3(a), demonstrating the elemental composition of PdO–2Mn_2O_3 with atomic% equivalent to the bulk in good agreement with the XRD analysis. Elemental mapping of Mn, Pd, and O exhibited the uniform distribution of all the elements.

The uniform arrangement of Pd, Mn and O over the whole area endorsed the presence of Pd, Mn and O in PdO–2Mn_2O_3 with uniformity.[53,54] In addition, the uniform arrangement of Pd, Mn and oxygen favors the electro-catalytic performance of PdO–2Mn_2O_3.[54]

The surface composition and oxidation states of the prepared PdO–2Mn_2O_3 material was probed by X-ray photoelectron spectroscopy (XPS). The survey spectrum (Fig. 4(a)) confirms Pd, Mn and O as the main constituent elements, in agreement with the EDX analysis. There is also a small N 1s peak at a binding energy of 400 eV, from the plant extract, and Mg contamination at the surface, but the origin of the Mg is unclear. Fig. 4(b) shows the core-level XPS Pd 3d spectrum. It is dominated by the spin–orbit split doublet peaks of Pd $3d_{5/2}$ and Pd $3d_{3/2}$ at binding energies (BE) of 337.3 eV and 342.6 eV, corresponding to an energy splitting of 5.3 eV, in good agreement with previous studies.[64–68] The spectra are also fitted with two additional sets of doublets that are assigned to shake-up satellites. The lower energies of these (BE = 340.2 and 345.5) have been assigned to charge transfer satellites due to interband transitions.[68] The origin of the higher energy satellites is less clear, but they are seen in the spectrum of oxidized palladium used as a PdO standard material in the work of Kibis *et al.*[68] We attribute these to multiplet type processes which occur due to the interaction of core-holes with valence electrons in Pd.

The Mn 2p XPS spectrum of the prepared Mn_2O_3 is shown in Fig. 4(c). The two features in the spectrum are the spin–orbit split Mn $2p_{3/2}$ and Mn $2p_{1/2}$ states, which appear at binding energies of 641.6 eV and 653.3 eV with an expected energy splitting value of doublet binding energy with an expected energy splitting value of 11.7 eV. As has been well documented, experimentally by the group of Biesinger *et al.*[69,70] and *via* the theoretical studies of Gupta and Sen,[71] transition metal 2p spectra are complex due to their multiplet structure. This occurs due to the interaction of the core-holes formed during the photoemission process with the valence electrons. Here we have used the multiplet peak structures with relative peak areas and energy separations for Mn_2O_3 (ref. 70) and achieve an excellent

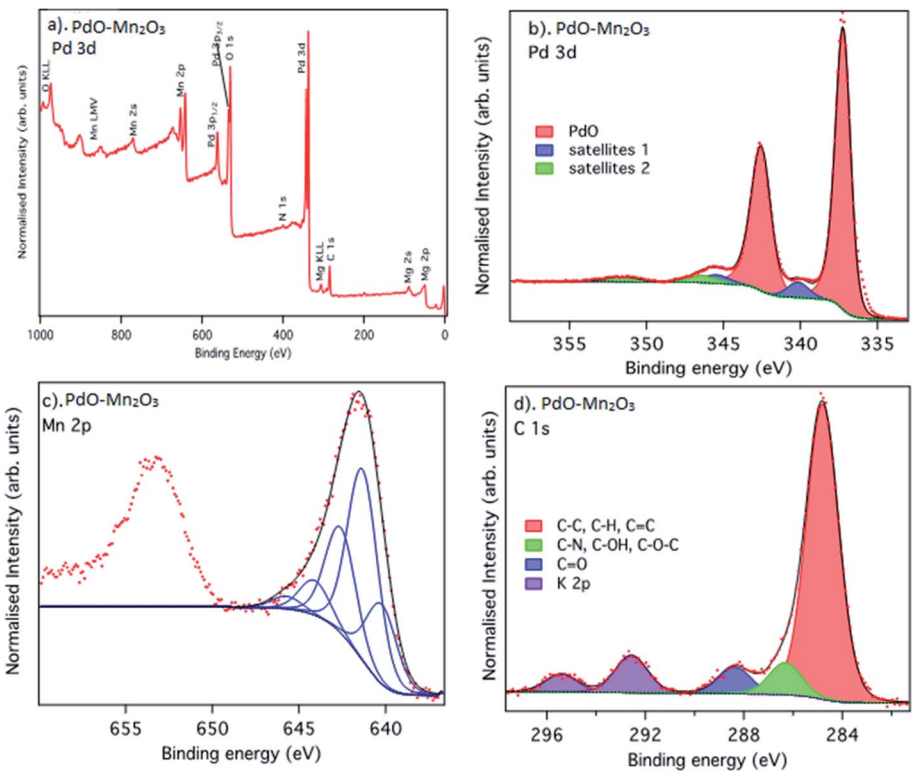

Fig. 4 XPS spectra recorded from PdO–2Mn_2O_3: (a) survey spectra, (b) Pd 3d, (c) Mn 2p, (d) C 1s core levels.

fit to the experimental data and therefore confirm the surface chemistry of the synthesized material to be consistent with Mn_2O_3. The Mn 2p spectrum is fitted according to the multiplet splitting suggested by Biesinger *et al.* for Mn_2O_3 (ref. 70, 95 and 96) and shows very good agreement.

We also note that the O 1s spectrum (see ESI†) is consistent with the presence of metal oxides at the surface. The O 1s spectrum shown in Fig. S2† is fitted with two peaks. The narrower peak at a binding energy (BE) centered at 530.2 eV is characteristic of metal oxides. We note that the peak is rather broad, with an FWHM of ~2 eV which may be indicative of the presence of the two different oxides in the material. The broad peak centered at a BE of ~534 eV is simply qualitative since this region of the spectrum is complex. Here there is overlap with the Pd $3p_{3/2}$ peak as well as a signal from organic oxygen-containing species and potentially from hydroxides and adsorbed water. Since the relative amounts of these species are not known, we have not attempted to fit peaks for the individual components. It is clear, however, that there are a significant number of O-containing species in this region, consistent with the presence of plant extract components on the surface of the PdO–Mn_2O_3 material.

The C 1s spectrum in Fig. 3(d) shows three distinctive peaks at 284.8 eV, 286.4 eV, and 288.5 eV, corresponding to C–C and C–H, C–OH/C–O–C/–C–N and C═O, respectively,[72] as well as some K 2p contamination from the synthesis process[73] ($2p_{3/2}$ and $2p_{1/2}$ spin–orbit split peaks at BE = 292.6 eV and 294.5 eV, respectively). A small peak is observed at a BE of 400 eV in the survey spectrum, corresponding to N 1s, indicating the presence of C–N species, as would be expected from bio-organic material.

The C 1s spectrum, therefore, confirms the presence of organic species at the surface of the synthesised materials. Although it is well established that exposure to atmospheric conditions leads to absorption of so-called atmospheric adventitious hydrocarbon, the relative abundance of the CO-containing species is higher than would be expected from atmospheric contamination, and C–N species are rarely seen in adventitious hydrocarbon. This then indicates that the plant phytochemicals are present at the surface and may act as stabilising molecules. In summary, the XPS analysis confirms the formation of Mn_2O_3 and PdO, as well as indicating the presence of carbonyl, C–N and C–OH on the surface of the sample related to the organic capping agents of the OFR.

Furthermore, the morphology of as-prepared PdO–$2Mn_2O_3$ nanoparticles was studied by FESEM (a and b) at different magnifications and TEM (c), as shown in Fig. 5. The images present an interconnected network of nanostructures with increased surface area, which facilitates excellent electrochemical conductivity or catalytic diffusion of ions. The uniform distribution of particles with a tubular shape *via* a facile greener synthesis route is the innovation of our work. In TEM it can be seen that particles are capped by phyto-capping agents. The darker tones in the TEM image represent catalyst particles, whereas the lighter fringes around them can be attributed to capping agents.

Band gap energy

The absorption spectrum of bio-synthesized PdO–$2Mn_2O_3$ is shown in Fig. 6. The absorption band revealed at 366 nm indicates the red shift of the nanoparticles. A sharp peak at 271 nm indicates the presence of a blue shift along with a bathochromic shift, and this blue shift is a suggestion of phytocompounds in the synthesized particles.

The band energy of fabricated PdO–$2Mn_2O_3$ was calculated from the absorption spectrum by using the Tauc plot presented in Fig. 6 (inset). Using the following relation, the band gap has been derived as:

$$\alpha h\nu = B(h\nu - E_g)^{\gamma}$$

where α is the absorption coefficient, $h\nu$ is the incident photon energy, E_g is the optical band gap energy, B is band tailing parameter, and γ is an index with different values for direct (1/2) and indirect (2) band gaps.

The corresponding band gap energy was 3.18 eV for phyto-capped PdO–$2Mn_2O_3$ from the band edge absorption peak as well as by the Tauc equation.

Electrochemical characterization

The catalytic behavior of a PdO–$2Mn_2O_3$/Ni-foam catalyst was investigated in 1 M KOH solution at a 1 mV s^{-1} sweep rate for OER at potentials ranging from 0 to 0.6 V (*vs.* RHE) and the results are shown in Fig. 7. Ni-foam was used in the present investigation just as the mechanical support and for collection of current, so it has no contribution to the catalytic working of the electrode. Linear sweep voltammetry was performed to validate the catalytic performance of the synthesized PdO–

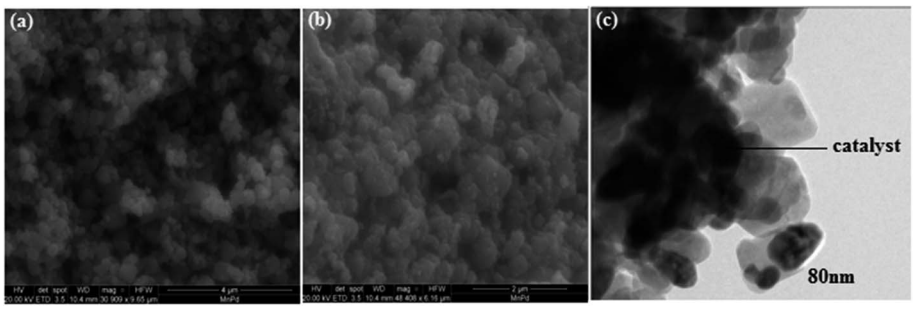

Fig. 5 (a and b) SEM micrographs at two different magnifications and (c) TEM image of PdO–$2Mn_2O_3$.

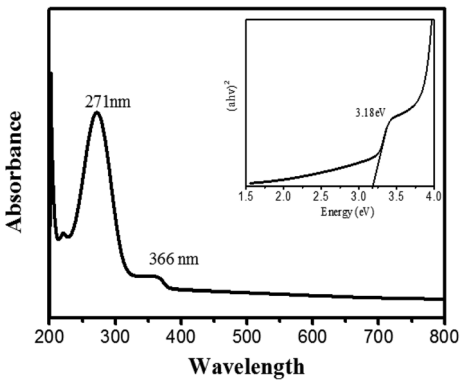

Fig. 6 Optical analysis of PdO–2Mn_2O_3 by UV-vis absorption spectra.

$2Mn_2O_3$. It was observed that the onset potential (RHE) of the oxygen evolution reaction was 1.58 V and the corresponding over-potential was 0.359 V (359 mV) to achieve an OER current density of 10 mA cm^{-2}. The results have been compared with previously reported studies, as given in Table 1. The Tafel slope of the prepared catalyst is a major indicator to demonstrate the electrochemical performance for oxygen evolution. The Tafel slope has been measured from the linear part of the curve potential (RHE) and current density, as shown in Fig. 7(b), which indicated good OER activity. The value of the Tafel slope was 115 mV dec^{-1}. The Tafel value in the present study is lower than the Tafel value of RuO_2 (128 mV dec^{-1}) in a study reported by Han *et al.*[74] In another study by Qayoom Mugheri *et al.*, RuO_2 shows a Tafel value of 161 mV dec^{-1}.[75] It has been assessed from the lower Tafel value that the synthesized material was deposited well on Ni-foam, exhibiting good OER performance. The smaller value of the Tafel slope indicates the enhanced and well-balanced kinetics during catalysis. Electrochemical impedance spectroscopy (EIS) was performed to further comprehend the charge transfer process at the interface of the fabricated electrode. The cumulative resistance of electrode material, electrolyte and electrolyte/electrode interface comes under R_s.[55] The impedance effect can be sub-divided further into high frequency regions (HFR) and low frequency regions (LFR). In the HFR, the intercept of the semicircle on the real axis denotes R_s and the width of the semicircle graph is representative of R_{ct}.[56] Whereas in the LFR, if the slope of impedance on the real axis is closer to a Warburg angle of 45° then it exhibits low Warburg impedance and improved ion transfer or diffusion from electrolyte to electrode, showing high capacitive behavior.[57]

A Randles circuit was employed for data fitting of every potential of the Nyquist plot (EIS) with R_{ct} values, as presented in Fig. 7(c) (inset S3a†). An equivalent circuit comprising two series-connected R_c elements is depicted in the figure to further

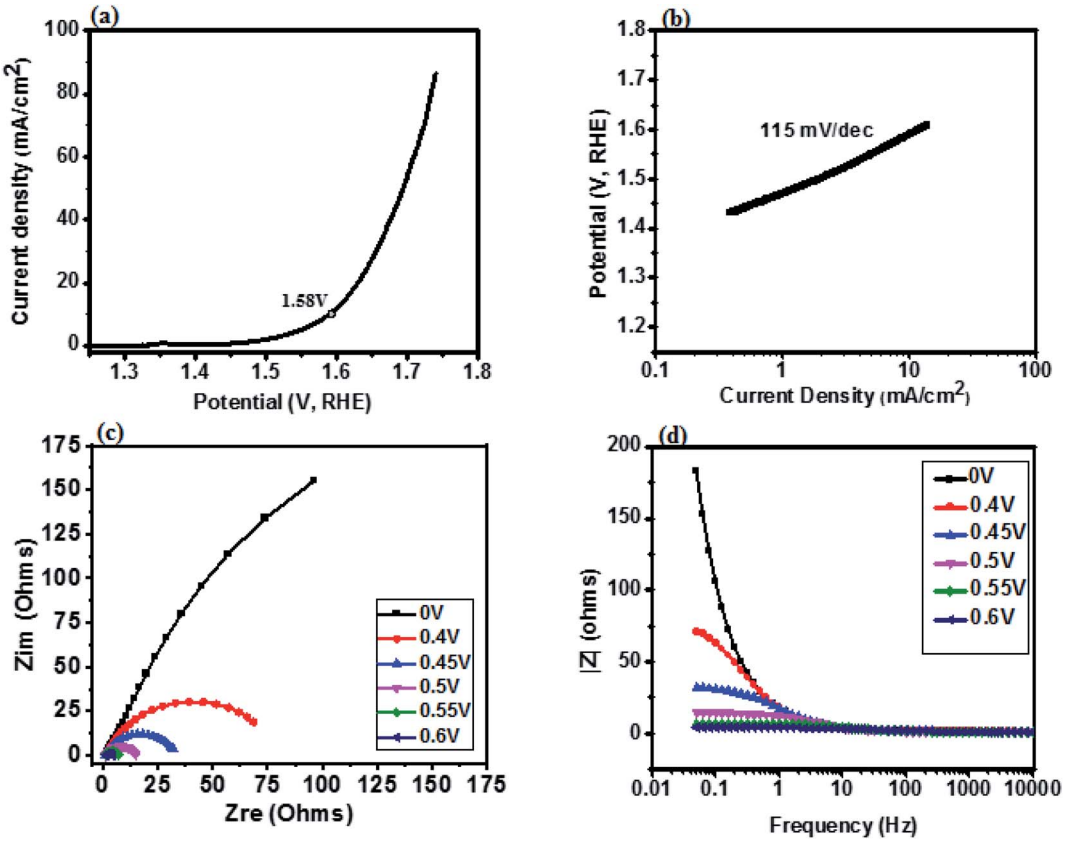

Fig. 7 Electro-catalytic measurements towards OER: (a) polarization curves, (b) Tafel slopes, (c) Nyquist plot at various potentials, (d) Bode plot showing variation in impedance as a function of frequency.

Table 1 The OER performance of PdO–2Mn_2O_3 catalyst in this work compared with other reported non-noble metal oxides in 1 M alkaline electrolyte

Catalyst	Overpotential at 10 mA cm^{-2}	Electrolyte	Tafel value (mV dec^{-1})	Ref.
$CoMnO_2$	390 mV	1 M KOH	95	77
Co_3O_4/$NiCo_2O_4$ DSNSCs	430	1 M KOH	—	78
Ni_2P nanoparticles	500	1 M KOH	—	80
$Co(PO_3)_2$ on Ni-foam	477	1 M KOH	—	82
PdO–2Mn_2O_3/Ni-foam	359 mV	1 M KOH	115	This work

interpret the EIS data. Just for a comparison at one only potential, *i.e.* 0.4 V, the data was fitted in an equivalent circuit (Fig. 8). The resistive and capacitive elements in this model have a direct relation with the charge transfer mechanism, which is correlated with water oxidation.[88,102] In the figure R_s is the overall resistance of the circuit, including the electrode resistance as well as the outer contact resistance of the EC cell. R_{sc} refers to the internal charge transfer resistance of the electrode, whereas R_{ct} exhibits the interfacial charge transfer resistance of electrode–electrolyte.

It was observed that the width of the semicircle is very small at higher potential (0.6 V), and the estimated R_{sc} and R_{ct} values were 1.103 Ω and 1.69 Ω, respectively, so it has small R_{sc} (internal resistance), which is attributed to the morphology of bio-fabricated Pd–Mn as well as to the presence of hydrophilic functional components of phytocompounds (oxygen species) on the surface, as vividly endorsed by the XPS analysis. The present employment is well supported by Wu *et al.* that phyto-capped metal oxides demonstrate efficient catalytic activity pertaining to the high surface area of the particles.[52,84] It is also supported by many other reports, according to which R_{sc} in the current study is much smaller than those of reported metal oxide based electrocatalysts.[17,85–87] Similarly, the R_{ct} value at 0.55 V was 3.41 Ω. With decreasing potential the semicircle got larger and then disappeared at low potentials. It can be assessed that in HFR the semicircle intercept is very small, indicating faradaic reaction driven charge transfer resistance. The inset in Fig. 7(c) (S3†) represents the HFR with a very small R_{ct} value at high potential. This is due to the faradaic reactions of Pd–Mn–O, as reported by previous studies[41,43,51,86,87] in which a small R_{ct} value favors efficient catalytic potential. As the Nyquist plot is indicative of charge transfer resistance, it represents the transfer of ions/charges between electrode and electrolyte interface. This means the resistance decreased with increasing potential, depicting good electrochemical transfer in terms of acceleration of the charge transfer between electrolyte and electrode. The minimum values of R_{ct} and R_{sc} depict higher diffusion and a charge transfer pathway exhibiting good electrochemical performance.

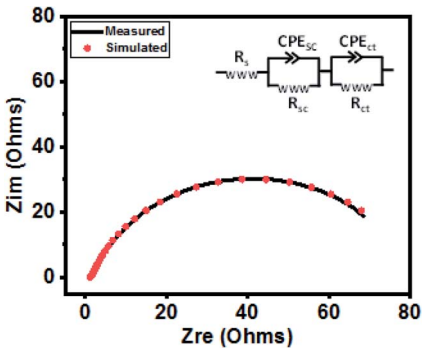

Fig. 8 The measured and simulated data for the sample measured at 0.4 V. The inset figure shows the equivalent circuit used for data fitting.

Fig. 7(d) represents the modulus of impedance *vs.* frequency on the *x*-axis with varied potential ranging from 0 to 0.6 V to understand the mechanism of charge transfer resistance. It was observed that 0 V, 0.4 V and 0.45 V showed almost the same response, having maximum impedance at lower frequency and decreasing with increasing frequency. At 0.55 V and 0.6 V impedance was about zero and it remained constant even with increasing frequency. This suggests that impedance was shifting towards the lower frequency region with increasing voltage, exhibiting fast electron conduction of PdO–2Mn_2O_3 consistent with the lower R_{ct} value. It can be seen that as the voltage increases, the impedance goes on decreasing to nearly zero, which depicts the good electrochemical performance of the electrode material.[39,58]

To further assess the potential of nickel foam supported PdO–2Mn_2O_3 as a bifunctional electrode material in water splitting, the same electrode material was tested for the hydrogen evolution reaction in 1 M KOH solution at different potentials ranging from −0.036 to −0.34 V (*vs.* RHE). As shown in Fig. 9(a), the PdO–2Mn_2O_3 electro-catalyst shows good performance with a small over-potential of 121 mV to attain a current density of 10 mA cm^{-2} which was close to that of state-of-the-art catalysts.

The calculated Tafel slope was 219 mV dec^{-1}, which is more than 115 mV dec^{-1}, exhibiting PdO–2Mn_2O_3 as more efficient for oxygen and oxide adsorption with enhanced kinetics in comparison to HER. The outcomes of the present investigation have been compared with previously reported studies on non-noble metals/metal oxides, as delineated in Table 2.

EIS measurements towards HER were undertaken and are shown in Fig. 9(c) in term of the Nyquist plot. It was observed that the width of the semicircle is very small at potential 0.34 V with an R_{ct} value of 2.44 Ω. With decreasing potential the semicircle became larger up to 0.036 V with an R_{ct} value of 25 Ω.

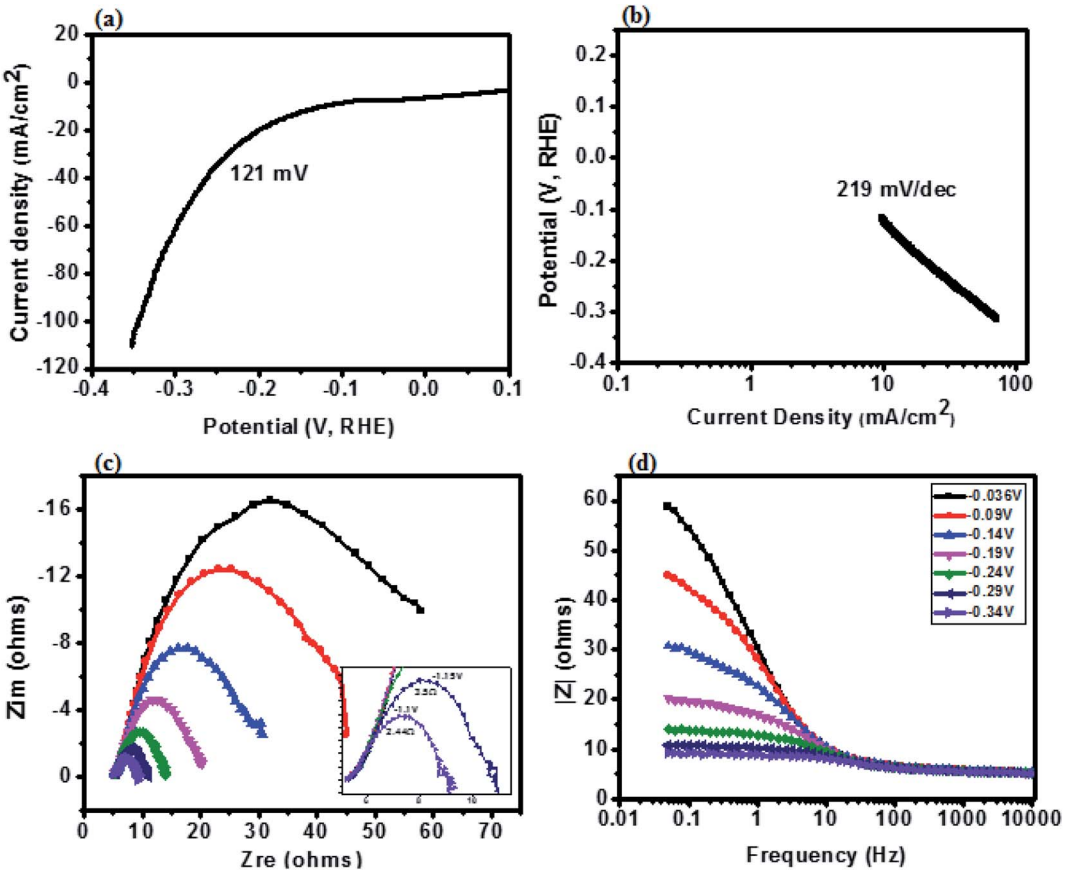

Fig. 9 Electro-catalytic measurements towards HER: (a) polarization curves, (b) Tafel slopes, (c) Nyquist plot at various potentials, (d) Bode plot showing variation in impedance as a function of frequency.

It can be assessed that in HFR the width of the semicircle is very small, indicating faradaic reaction driven charge transfer resistance. This suggests good electrochemical performance in term of charge transfer between electrode and electrolyte.[97,103] The Bode plot (Fig. 9(d)) between impedance and frequency suggests that the impedance was shifting towards the lower frequency region with increasing voltage, exhibiting the fast electron conduction of PdO–2Mn_2O_3, in good agreement with the lower value of R_{ct}. It can be seen that with an increase in voltage, impedance decreases and becomes closer to 8 Ω from 60 Ω, which depicts the good electrochemical performance of the electrode material.[63,98]

The active functioning of PdO–2Mn_2O_3 as a more efficient electro-catalyst for the OER is mainly due two reasons: the introduction of PdOx with Mn_2O_3 which produces a synergic effect on the overall efficiency of the electrode material and, secondly, the organic phytocompounds or carbon-containing capping agents used in the synthesis of the oxides which has been confirmed by XPS and GC-MS analysis ($C_{10}H_{20}O_2$). By introducing any dopant, activity could be enhanced by providing more active sites and charge carriers.[59] On the basis of previous studies it has come to be known that palladium is an electroactive OER catalytic material compared to Pt or Ir_2, as reported by Joya *et al.*, Wang *et al.* and Fang *et al.*[89–91] Secondly, the present manipulation has been made on the basis of an

Table 2 The HER performance of the PdO–2Mn_2O_3 catalyst in this work compared with other reported non-noble metal oxides in 1 M alkaline electrolyte

Catalyst	Over-potential at 10 mA cm^{-2}	Electrolyte	Supporting substrate	Ref.
NiFe-LDH/$NiCo_2O_4$	192 mV	1 M KOH	Ni-foam	78
PA-NiO	138 mV	1 M KOH	Ni-foam	79
MnNi	360 mV	1 M KOH	Ni-foam	81
$Fe_{0.5}Co_{0.5}$@NC/NCNS	150 mV	1 M KOH	Ni-foam	83
PdO–2Mn_2O_3	121 mV	1 M KOH	Ni-foam	This work

assessment (ESI Fig. 4(a) and (b)†) in which Mn_2O_3 has been tested individually for OER and HER activity. The findings gave an over-potential value of 431 mV for OER, whereas they gave a very poor performance towards HER. So manganese oxide has been doped by PdO to improve the catalytic efficiency of the electro-catalyst by its synergistic behavior. In addition, mass loading also has a positive effect on the catalytic performance of the material, as with an increase in mass loading, the response of catalyst would be more prominent in terms of minimizing the effect of the substrate. With reference to published studies,[86,93,94] 2 mg mass loading was chosen to maximize the energy generation capability of the catalyst. Previously, pure manganese and palladium oxide synthesized by chemical or physical approaches have been used largely due to their electro-efficient behavior in electrochemical reactions, but *Olea ferruginea* Royle fabricated palladium and manganese oxide has not been used for electrochemical reactions. Thus it is strongly comprehended that the current approach is most favorable in term of cost as well as in terms of toxicity. In addition, Gul and Ahmad reported that carbon-containing species played important roles which enhance the electron flow and current carriers[60–62,99] by the following mechanism occurring at the anode and cathode:

$$\text{Organic compounds + water} \rightarrow CO_2 + H^+ + e^- \text{ at the anode}$$

$$O_2 + H^+ + e^- \rightarrow H_2O \text{ at the cathode}$$

Thus in the present work, carbon-containing species perform in the electrochemical reaction according to the following equation:

$$C + H_2O \rightarrow CO_2 + 4H^+ + 4e^- \text{ at the anode}$$

$$4H^+ + 4e^- \rightarrow H_2 \text{ at the cathode}$$

The HER performance of PdO–2Mn_2O_3 was much better than the HER of individual MnO (ESI Fig. 4c and d†) which gives an over-potential of 162 mV and a Tafel value of 395 mV dec^{-1}; such a high Tafel slope value is due to electron poisoning which hinders the movement of charges. However, according to the literature,[89,91,92] PdO is more efficient for OER activity and thus the present findings are more favorable for the OER.

Conclusion

PdO–2Mn_2O_3 supported on Ni-foam was fabricated by a phyto-synthesized greener and cost-effective route using a leaf extract of the *Olea ferruginea* Royle plant. Prior to electrochemical scrutinization, the as-synthesized composite material was characterized by FTIR, GC-MS, XRD, XPS, SEM, TEM and EDX analysis. The results imply formation of PdO and Mn_2O_3 nano-crystallites with crystallite sizes of 15.44 and 14.55 nm, respectively. The electrochemical performance of the synthesized material was studied and it was found that the material behaves as a bifunctional electro-catalyst for both OER and HER performance with low over-potential and Tafel slope, indicating fast electron transfer. Furthermore, the present method is most favorable in terms of commercial and environmental cost as a greener and environmentally benign electrode material as an alternative to the chemical synthesis route. The phyto-functionalized electrode material is a step towards environmental remediation and sustainable development in terms of renewable energy, which can be explored further following the present investigation.

Conflicts of interest

The authors declare no conflict of interest.

Acknowledgements

The authors acknowledge the faculty of Fatima Jinnah Women University, Rawalpindi, Pakistan, Higher education commission of Pakistan (HEC) and University of Manchester, UK for synthesis and characterization. The authors also acknowledge Dr Ram Gupta, Polymer Chemistry Program and the Kansas Polymer Research Center, Pittsburg State University, USA for electrochemical testing and assistance. The concept, idea, data and writing is the intellectual property right of Dr Khuram Shahzad Ahmad and Lab E-21 of Department of Environmental Sciences, Fatima Jinnah Women University, The Mall, 46000, Rawalpindi, Pakistan.

References

1 C. Wang, F. Hu, H. Yang, Y. Zhang, H. Lu and Q. Wang, 1.82 wt.% Pt/N, P co-doped carbon overwhelms 20 wt.% Pt/C as a high-efficiency electrocatalyst for hydrogen evolution reaction, *Nano Res.*, 2017, **10**(1), 238–246.
2 M. Zhang, M. De Respinis and H. Frei, Time-resolved observations of water oxidation intermediates on a cobalt oxide nanoparticle catalyst, *Nat. Chem.*, 2014, **6**(4), 362–367.
3 M. I. Jamesh, Recent progress on earth abundant hydrogen evolution reaction and oxygen evolution reaction bifunctional electrocatalyst for overall water splitting in alkaline media, *J. Power Sources*, 2016, **333**, 213–236.
4 X. Wang, W. Gao, Z. Zhao, L. Zhao, J. P. Claverie, X. Zhang, J. Wang, H. Liu and Y. Sang, Efficient photo-electrochemical water splitting based on hematite nanorods doped with phosphorus, *Appl. Catal., B*, 2019, **248**, 388–393.
5 Y. Li, H. Zhang, M. Jiang, Y. Kuang, X. Sun and X. Duan, Ternary NiCoP nanosheet arrays: An excellent bifunctional catalyst for alkaline overall water splitting, *Nano Res.*, 2016, **9**(8), 2251–2259.
6 Y. Li, H. Zhang, T. Xu, Z. Lu, X. Wu, P. Wan, X. Sun and L. Jiang, Under-water superaerophobic pine-shaped Pt nanoarray electrode for ultrahigh-performance hydrogen evolution, *Adv. Funct. Mater.*, 2015, **25**(11), 1737–1744.
7 S. Q. Wang, W. Y. Xia, Z. S. Liang, Z. L. Liu, C. W. Xu and Q. Y. Li, NiO/C enhanced by noble metal (Pt, Pd, Au) as high-efficient electrocatalyst for oxygen evolution reaction

in water oxidation to obtain high purity hydrogen, *Ionics*, 2017, **23**(8), 2161–2166.

8 R. E. Fuentes, J. Farell and J. W. Weidner, Electrochemical Synthesis and Engineering Multimetallic Electrocatalysts of Pt, Ru, and Ir Supported on Anatase and Rutile TiO2 for Oxygen Evolution in an Acid Environment, *Electrochem. Solid-State Lett.*, 2011, **14**(3), E5.

9 W. Hu, Y. Wang, X. Hu, Y. Zhou and S. Chen, Three-dimensional ordered macroporous IrO 2 as electrocatalyst for oxygen evolution reaction in acidic medium, *J. Mater. Chem.*, 2012, **22**(13), 6010–6016.

10 R. Li, Z. Wei and X. Gou, Nitrogen and phosphorus dual-doped graphene/carbon nanosheets as bifunctional electrocatalysts for oxygen reduction and evolution, *ACS Catal.*, 2015, **5**(7), 4133–4142.

11 X. Zhou, Y. Liu, H. Ju, B. Pan, J. Zhu, T. Ding, C. Wang and Q. Yang, Design and epitaxial growth of MoSe2–NiSe vertical heteronanostructures with electronic modulation for enhanced hydrogen evolution reaction, *Chem. Mater.*, 2016, **28**(6), 1838–1846.

12 G. Kwon, G. A. Ferguson, C. J. Heard, E. C. Tyo, C. Yin, J. DeBartolo, S. Seifert, R. E. Winans, A. J. Kropf, J. Greeley and R. L. Johnston, Size-dependent subnanometer Pd cluster (Pd4, Pd6, and Pd17) water oxidation electrocatalysis, *ACS Nano*, 2013, **7**(7), 5808–5817.

13 L. Bao, J. Zang and X. Li, Flexible Zn2SnO4/MnO2 core/shell nanocable− carbon microfiber hybrid composites for high-performance supercapacitor electrodes, *Nano Lett.*, 2011, **11**(3), 1215–1220.

14 Z. S. Wu, W. Ren, D. W. Wang, F. Li, B. Liu and H. M. Cheng, High-energy MnO2 nanowire/graphene and graphene asymmetric electrochemical capacitors, *ACS Nano*, 2010, **4**(10), 5835–5842.

15 N. Duraisamy, A. Numan, S. O. Fatin, K. Ramesh and S. Ramesh, Facile sonochemical synthesis of nanostructured NiO with different particle sizes and its electrochemical properties for supercapacitor application, *J. Colloid Interface Sci.*, 2016, **471**, 136–144.

16 C. Zhou, Y. Zhang, Y. Li and J. Liu, Construction of high-capacitance 3D CoO@ polypyrrole nanowire array electrode for aqueous asymmetric supercapacitor, *Nano Lett.*, 2013, **13**(5), 2078–2085.

17 Y. Meng, W. Song, H. Huang, Z. Ren, S. Y. Chen and S. L. Suib, Structure–property relationship of bifunctional MnO2 nanostructures: highly efficient, ultra-stable electrochemical water oxidation and oxygen reduction reaction catalysts identified in alkaline media, *J. Am. Chem. Soc.*, 2014, **136**(32), 11452–11464.

18 M. M. Najafpour, F. Rahimi, M. Amini, S. Nayeri and M. Bagherzadeh, A very simple method to synthesize nano-sized manganese oxide: an efficient catalyst for water oxidation and epoxidation of olefins, *Dalton Trans.*, 2012, **41**(36), 11026–11031.

19 X. Gao, H. Zhang, Q. Li, X. Yu, Z. Hong, X. Zhang, C. Liang and Z. Lin, Hierarchical NiCo2O4 hollow microcuboids as bifunctional electrocatalysts for overall water-splitting, *Angew. Chem., Int. Ed.*, 2016, **55**(21), 6290–6294.

20 E. Rios, J. L. Gautier, G. Poillerat and P. Chartier, Mixed valency spinel oxides of transition metals and electrocatalysis: case of the MnxCo3− xO4 system, *Electrochim. Acta*, 1998, **44**(8–9), 1491–1497.

21 X. Liu, Z. Chang, L. Luo, T. Xu, X. Lei, J. Liu and X. Sun, Hierarchical Zn x Co3–x O4 Nanoarrays with High Activity for Electrocatalytic Oxygen Evolution, *Chem. Mater.*, 2014, **26**(5), 1889–1895.

22 M. De Koninck, S. C. Poirier and B. Marsan, Cu x Co3− x O4 Used as Bifunctional Electrocatalyst: Physicochemical properties and electrochemical characterization for the oxygen evolution reaction, *J. Electrochem. Soc.*, 2006, **153**(11), A2103.

23 O. V. Kharissova, H. R. Dias, B. I. Kharisov, B. O. Pérez and V. M. Pérez, The greener synthesis of nanoparticles, *Trends Biotechnol.*, 2013, **31**(4), 240–248.

24 A. Siromani, K. Daniel, G. Singhal, R. Bhavesh, K. Kasaraiya, A. R. Sharma and R. P. Singh, Biosynthesis of silver nanoparticles using Ocimum sanctum (Tulsi) leaf extract and screening its antimicrobial activity, *J. Nanopart. Res.*, 2011, **13**, 2981–2988.

25 M. N. Nadagouda, G. Hoag, J. Collins and R. S. Varma, Green synthesis of Au nanostructures at room temperature using biodegradable plant surfactants, *Cryst. Growth Des.*, 2009, **9**(11), 4979–4983.

26 M. Shah, D. Fawcett, S. Sharma, S. K. Tripathy and G. E. Poinern, Green synthesis of metallic nanoparticles via biological entities, *Materials*, 2015, **8**(11), 7278–7308.

27 N. J. Sushma, D. Prathyusha, G. Swathi, T. Madhavi, B. D. Raju, K. Mallikarjuna and H. S. Kim, Facile approach to synthesize magnesium oxide nanoparticles by using Clitoria ternatea—characterization and in vitro antioxidant studies, *Appl. Nanosci.*, 2016, **6**(3), 437–444.

28 A. Leela and M. Vivekanandan, Tapping the unexploited plant resources for the synthesis of silver nanoparticles, *Afr. J. Biotechnol.*, 2008, **7**(17), 3162–3165.

29 H. Genuino, H. Huang, E. Njagi, L. Stafford and S. L. Suib, A review of green synthesis of nanophase inorganic materials for green chemistry applications, *Handbook of Green Chemistry*, 2010, pp. 217–244.

30 E. O. Dare, C. O. Oseghale, A. H. Labulo, E. T. Adesuji, E. E. Elemike, J. C. Onwuka and J. T. Bamgbose, Green synthesis and growth kinetics of nanosilver under bio-diversified plant extracts influence, *J. Nanostruct. Chem.*, 2015, **5**(1), 85–94.

31 J. H. Kim, J. W. Jang, H. J. Kang, G. Magesh, J. Y. Kim, J. H. Kim, J. Lee and J. S. Lee, Palladium oxide as a novel oxygen evolution catalyst on BiVO4 photoanode for photoelectrochemical water splitting, *J. Catal.*, 2014, **317**, 126–134.

32 S. Sarkar and S. C. Peter, An overview on Pd-based electrocatalysts for the hydrogen evolution reaction, *Inorg. Chem. Front.*, 2018, **5**(9), 2060–2080.

33 H. He, J. Chen, D. Zhang, F. Li, X. Chen, Y. Chen and X. Lv, Modulating the electrocatalytic performance of palladium with the electronic metal–support interaction: a case

study on oxygen evolution reaction, *ACS Catal.*, 2018, **8**(7), 6617–6626.

34 M. A. Hashmi, H. S. Shah, A. Khan, U. Farooq, J. Iqbal, V. U. Ahmad and S. Perveen, Anticancer and alkaline phosphatase inhibitory effects of compounds isolated from the leaves of Olea ferruginea Royle, *Rec. Nat. Prod.*, 2015, **9**(1), 164.

35 S. Z. Siddiqui, M. A. Abbasi, T. Riaz, T. Shahzadi, M. Ajaib and K. M. Khan, Olea ferrugenia: A potential natural source of protection from oxidative stress, *J. Med. Plants Res.*, 2011, **5**(17), 4080–4086.

36 M. Ndikau, N. M. Noah, D. M. Andala and E. Masika, Green synthesis and characterization of silver nanoparticles using Citrullus lanatus fruit rind extract, *Int. J. Anal. Chem.*, 2017, **2017**, 8108504.

37 L. Ortega-Arroyo, E. S. Martin-Martinez, M. A. Aguilar-Mendez, A. Cruz-Orea, I. Hernandez-Pérez and C. Glorieux, Green synthesis method of silver nanoparticles using starch as capping agent applied the methodology of surface response, *Starch/Staerke*, 2013, **65**(9–10), 814–821.

38 K. Sivanesan, P. Jayakrishnan, S. Abdul Razack, P. Sellaperumal, G. Ramakrishnan and R. Sahadevan, Biofabrication of manganese nanoparticle using Aegle marmelos fruit extract and assessment of its biological activities, *Nanomed. Res. J.*, 2017, **2**(3), 171–178.

39 C. Gervas, M. D. Khan, S. Mlowe, C. Zhang, C. Zhao, R. K. Gupta and N. Revaprasadu, Synthesis of Off-Stoichiometric CoS Nanoplates from a Molecular Precursor for Efficient H2/O2 Evolution and Supercapacitance, *ChemElectroChem*, 2019, **6**(9), 2560–2569.

40 M. Hou, and J. Ge, Armoring enzymes by metal–organic frameworks by the coprecipitation method, in *Methods in enzymology*, Academic Press, 2017, vol. 590, pp. 59–75.

41 L. Kang, S. X. Sun, L. B. Kong, J. W. Lang and Y. C. Luo, Investigating metal-organic framework as a new pseudo-capacitive material for supercapacitors, *Chin. Chem. Lett.*, 2014, **25**(6), 957–961.

42 A. Kumar and M. Khandelwal, A novel synthesis of ultra thin graphene sheets for energy storage applications using malonic acid as a reducing agent, *J. Mater. Chem. A*, 2014, **2**(47), 20345–20357.

43 J. H. Kim, J. W. Jang, H. J. Kang, G. Magesh, J. Y. Kim, J. H. Kim and J. S. Lee, Palladium oxide as a novel oxygen evolution catalyst on BiVO4 photoanode for photoelectrochemical water splitting, *J. Catal.*, 2014, **317**, 126–134.

44 K. M. Parida and B. Naik, Synthesis of mesoporous TiO2−xNx spheres by template free homogeneous co-precipitation method and their photo-catalytic activity under visible light illumination, *J. Colloid Interface Sci.*, 2009, **333**(1), 269–276.

45 K. Geethalakshmi, T. Prabhakaran and J. Hemalatha, Dielectric studies on nano zirconium dioxide synthesized through co-precipitation process, *World Acad. Sci. Eng. Technol.*, 2012, **64**, 179–182.

46 Ş. Ş. Türkyılmaz, N. Güy and M. Özacar, Photocatalytic efficiencies of Ni, Mn, Fe and Ag doped ZnO nanostructures synthesized by hydrothermal method: The synergistic/antagonistic effect between ZnO and metals, *J. Photochem. Photobiol., A*, 2017, **341**, 39–50.

47 K. S. Ahmad and S. B. Jaffri, Phytosynthetic Ag doped ZnO nanoparticles: Semiconducting green remediators, *Open Chem.*, 2018, **16**(1), 556–570.

48 X. Peng, X. Bai, Z. Cui and X. Liu, Green synthesis of Pd truncated octahedrons using of firmiana simplex leaf extract and their catalytic study for electro-oxidation of methanol and reduction of p-nitrophenol, *Appl. Organomet. Chem.*, 2019, e5045.

49 R. S. S. Kumar, S. Murugesan, G. Kottur, and D. Gyamfi, Black tea: The plants, processing/manufacturing and production, *Tea in health and disease prevention*, 2013, pp. 41–57.

50 K. Vijayaraghavan, S. K. Nalini, N. U. Prakash and D. Madhankumar, One step green synthesis of silver nano/microparticles using extracts of Trachyspermum ammi and Papaver somniferum, *Colloids Surf., B*, 2012, **94**, 114–117.

51 I. Shaheen, K. S. Ahmad, C. Zequine, R. K. Gupta, A. G. Thomas and M. A. Malik, Effect of NiO on organic framework functionalized ZnO nanoparticles for energy storage application, *Int. J. Energy Res.*, 2020, **44**(7), 5259–5271.

52 J. Theerthagiri, K. Thiagarajan, B. Senthilkumar, Z. Khan, R. A. Senthil, P. Arunachalam and M. Ashokkumar, Synthesis of hierarchical cobalt phosphate nanoflakes and their enhanced electrochemical performances for supercapacitor applications, *ChemistrySelect*, 2017, **2**(1), 201–210.

53 P. Iamprasertkun, A. Krittayavathananon, A. Seubsai, N. Chanlek, P. Kidkhunthod, W. Sangthong and S. Ittisanronnachai, Charge storage mechanisms of manganese oxide nanosheets and N-doped reduced graphene oxide aerogel for high-performance asymmetric supercapacitors, *Sci. Rep.*, 2016, **6**, 37560.

54 B. V. Krishna, J. Bhagwan and J. S. Yu, Sol-Gel Routed NiMn2O4 Nanofabric Electrode Materials for Supercapacitors, *J. Electrochem. Soc.*, 2019, **166**(10), A1950–A1955.

55 P. Song, D. Wen, Z. X. Guo and T. Korakianitis, Oxidation investigation of nickel nanoparticles, *Phys. Chem. Chem. Phys.*, 2008, **10**(33), 5057–5065.

56 S. K. Meher and G. R. Rao, Enhanced activity of microwave synthesized hierarchical MnO2 for high performance supercapacitor applications, *J. Power Sources*, 2012, **215**, 317–328.

57 C. W. Huang and H. Teng, Influence of carbon nanotube grafting on the impedance behavior of activated carbon capacitors, *J. Electrochem. Soc.*, 2008, **155**(10), A739–A744.

58 S. Khalid, C. Cao, L. Wang and Y. Zhu, Microwave assisted synthesis of porous NiCo 2 O 4 microspheres: application as high performance asymmetric and symmetric

supercapacitors with large areal capacitance, *Sci. Rep.*, 2016, **6**, 22699.

59 S. Anantharaj, M. Venkatesh, A. S. Salunke, T. V. Simha, V. Prabu and S. Kundu, High-performance oxygen evolution anode from stainless steel via controlled surface oxidation and Cr removal, *ACS Sustainable Chem. Eng.*, 2017, **5**(11), 10072–10083.

60 Y. Hou, M. R. Lohe, J. Zhang, S. Liu, X. Zhuang and X. Feng, Vertically oriented cobalt selenide/NiFe layered-double-hydroxide nanosheets supported on exfoliated graphene foil: an efficient 3D electrode for overall water splitting, *Energy Environ. Sci.*, 2016, **9**, 478–483.

61 H. Yan, C. Su, J. He and W. Chen, Single-atom catalysts and their applications in organic chemistry, *J. Mater. Chem. A*, 2018, **6**(19), 8793–8814.

62 M. M. Gul and K. S. Ahmad, Bioelectrochemical systems: Sustainable bio-energy powerhouses, *Biosens. Bioelectron.*, 2019, 111576.

63 L. S. Ferreira, T. R. Silva, J. R. Santos, V. D. Silva, R. A. Raimundo, M. A. Morales and D. A. Macedo, Structure, magnetic behavior and OER activity of CoFe2O4 powders obtained using agar-agar from red seaweed (Rhodophyta), *Mater. Chem. Phys.*, 2019, **237**, 121847.

64 C. D. Wagner, A. V. Naumkin, A. Kraut-Vass, J. W. Allison, C. J. Powell Jr and J. R. Rumble, *NIST Standard Reference Database 20*, Version 3.4 (web version), 2003, http:/srdata.nist.gov/xps/.

65 J. F. Moulder, W. F. Stickle, P. E. Sobol and K. D. Bomben, *Handbook of X-ray Photoelectron Spectroscopy*, PerkinElmer Corp., Eden Prairie, MN, 1992.

66 G. B. Hoflund, H. A. E. Hagelin, J. F. Weaver and G. N. Salaita, ELS and XPS study of Pd/PdO methane oxidation catalysts, *Appl. Surf. Sci.*, 2003, **205**, 102–112.

67 M. Brun, A. Berthet and J. C. Bertolini, XPS, AES and Auger parameter of Pd and PdO, *J. Electron Spectrosc. Relat. Phenom.*, 1999, **104**, 55–60.

68 L. S. Kibis, A. I. Titkov, A. I. Stadnichenko, S. V. Koscheev and A. I. Boronin, *Appl. Surf. Sci.*, 2009, **255**, 9248–9254.

69 M. C. Biesinger, L. W. M. Lau, A. R. Gerson and R. S. C. Smart, *Appl. Surf. Sci.*, 2010, **257**, 887–898.

70 M. C. Biesinger, B. P. Payne, A. P. Grosvenor, L. W. M. Lau, A. R. Gerson and R. S. C. Smart, *Appl. Surf. Sci.*, 2011, **257**, 2717–2730.

71 R. P. Gupta and S. K. Sen, *Phys. Rev. B: Solid State*, 1975, **12**, 15–19.

72 M. Wagstaffe, H. Hussain, M. Taylor, M. Murphy, N. Silikas and A. G. Thomas, *Mater. Sci. Eng., C*, 2019, **105**, 110030.

73 A. Miyakoshi, A. Ueno and M. Ichikawa, *Appl. Catal., A*, 2001, **219**, 249–258.

74 H. S. Han, K. M. Kim, H. Choi, G. Ali, K. Y. Chung, Y.-R. Hong, J. Choi, J. Kwon, S. W. Lee, J. W. Lee, J. H. Ryu, T. Song and S. Mhin, Parallelized Reaction Pathway and Stronger Internal Band Bending by Partial Oxidation of Metal Sulfide−Graphene Composites: Important Factors of Synergistic Oxygen Evolution Reaction Enhancement, *ACS Catal.*, 2018, 4091–4102.

75 A. Q. Mugheri, A. Tahira, U. Aftab, M. I. Abro, S. R. Chaudhry, L. Amaralde and Z. H. Ibupoto, Facile efficient earth abundant NiO/C composite electrocatalyst for the oxygen evolution reaction, *RSC Adv.*, 2019, 5701–5710.

76 M. C. Morris, *Standard X-ray Diffraction Powder Patterns: Section 16-data for 86 Substances*, Department of Commerce, National Bureau of Standards, 1979, vol. 25.

77 D. Li, H. Baydoun, C. N. Verani and S. L. Brock, Efficient water oxidation using CoMnP nanoparticles, *J. Am. Chem. Soc.*, 2016, **138**(12), 4006–4009.

78 Z. Wang, S. Zeng, W. Liu, X. Wang, Q. Li, Z. Zhao and F. Geng, Coupling Molecularly Ultrathin Sheets of NiFe-Layered Double Hydroxide on NiCo2O4Nanowire Arrays for Highly Efficient Overall Water-Splitting Activity, *ACS Appl. Mater. Interfaces*, 2017, **9**, 1488–1495.

79 Z. Li, W. Niu, L. Zhou and Y. Yang, Phosphorus and aluminum codoped porous NiO nanosheets as highly efficient electrocatalysts for overall water splitting, *ACS Energy Lett.*, 2018, **3**(4), 892–898.

80 A. Han, H. L. Chen, Z. J. Sun, J. Xu and P. W. Du, *Chem. Commun.*, 2015, **51**, 11626.

81 X. Wu, X. Han, X. Ma, W. Zhang, Y. Deng, C. Zhong and W. Hu, Morphology-controllable synthesis of Zn–Co-mixed sulfide nanostructures on carbon fiber paper toward efficient rechargeable zinc–air batteries and water electrolysis, *ACS Appl. Mater. Interfaces*, 2017, **9**(14), 12574–12583.

82 H. S. Ahn and T. D. Tilley, Electrocatalytic Water Oxidation at Neytral pH by a Nanostructured Co(PO3)2 Anode, *Adv. Funct. Mater.*, 2013, **23**, 227–233.

83 M. Li, T. Liu, X. Bo, M. Zhou and L. Guo, *J. Mater. Chem. A*, 2017, **5**, 5413.

84 H. Wu, Z. Lou, H. Yang and G. Shen, A flexible spiral-type supercapacitor based on ZnCo 2 O 4 nanorod electrodes, *Nanoscale*, 2015, **7**(5), 1921–1926.

85 D. Kong, Y. Wang, S. Huang, J. Hu, Y. Von Lim, B. Liu and H. Y. Yang, 3D self-branched zinc-cobalt Oxide@ N-doped carbon hollow nanowall arrays for high-performance asymmetric supercapacitors and oxygen electrocatalysis, *Energy Storage Materials*, 2019, 653–663.

86 C. Zequine, S. Bhoyate, F. Wang, X. Li, K. Siam, P. K. Kahol and R. K. Gupta, Effect of solvent for tailoring the nanomorphology of multinary CuCo2S4 for overall water splitting and energy storage, *J. Alloys Compd.*, 2019, **784**, 1–7.

87 H. Xiao, W. Guo, B. Sun, M. Pei and G. Zhou, Mesoporous TiO2 and Co-doped TiO2 nanotubes/reduced graphene oxide composites as electrodes for supercapacitors, *Electrochim. Acta*, 2016, **190**, 104–117.

88 Y. H. Chiu, T. H. Lai, C. Y. Chen, P. Y. Hsieh, K. Ozasa, M. Niinomi and Y. J. Hsu, Fully depleted Ti–Nb–Ta–Zr–O nanotubes: interfacial charge dynamics and solar hydrogen production, *ACS Appl. Mater. Interfaces*, 2018, **10**(27), 22997–23008.

89 K. S. Joya, M. A. Ehsan, M. Sohail and Z. H. Yamani, Nanoscale palladium as a new benchmark electrocatalyst

for water oxidation at low overpotential, *J. Mater. Chem. A*, 2019, **7**(15), 9137–9144.

90 Y. Fang, X. Li, Y. Hu, F. Li, X. Lin, M. Tian and J. Ma, Ultrasonication-assisted ultrafast preparation of multiwalled carbon nanotubes/Au/Co3O4 tubular hybrids as superior anode materials for oxygen evolution reaction, *J. Power Sources*, 2015, **300**, 285–293.

91 S. Q. Wang, W. Y. Xia, Z. S. Liang, Z. L. Liu, C. W. Xu and Q. Y. Li, NiO/C enhanced by noble metal (Pt, Pd, Au) as high-efficient electrocatalyst for oxygen evolution reaction in water oxidation to obtain high purity hydrogen, *Ionics*, 2017, **23**(8), 2161–2166.

92 M. A. Khan, H. Zhao, W. Zou, Z. Chen, W. Cao, J. Fang and J. Zhang, Recent progresses in electrocatalysts for water electrolysis, *Electrochem. Energy Rev.*, 2018, **1**(4), 483–530.

93 C. Zhang, S. Bhoyate, C. Zhao, P. K. Kahol, N. Kostoglou, C. Mitterer, S. J. Hinder, M. A. Baker, G. Constantinides, K. Polychronopoulou and C. Rebholz, Electrodeposited nanostructured CoFe2O4 for overall water splitting and supercapacitor applications, *Catalysts*, 2019, **9**(2), 176.

94 I. Shaheen, K. S. Ahmad, C. Zequine, R. K. Gupta, A. G. Thomas and M. A. Malik., Effect of NiO on organic framework functionalized ZnO nanoparticles for energy storage application, *Int. J. Energy Res.*, 2020, **44**(7), 5259–5271.

95 M. A. Stranick, *Surf. Sci. Spectra*, 1999, **6**(1), 39.

96 Y. Park, S. W. Lee, K. H. Kim, B.-K. Min, A. K. Nayak, D. Pradhan and Y. Sohn, *Sci. Rep.*, 2015, **5**(1), 18275.

97 M. Tayebi and B. K. Lee, Recent advances in BiVO4 semiconductor materials for hydrogen production using photoelectrochemical water splitting, *Renewable Sustainable Energy Rev.*, 2019, **111**, 332–343, DOI: 10.1016/j.rser.2019.05.030.

98 J. S. Kang, Y. Noh, J. Kim, H. Choi, T. H. Jeon, D. Ahn, *et al.*, Iron Oxide Photoelectrode with Multidimensional Architecture for Highly Efficient Photoelectrochemical Water Splitting, *Angew. Chem., Int. Ed.*, 2017, **56**, 6583–6588, DOI: 10.1002/anie.201703326.

99 Y. Chen, X. Feng, Y. Liu, X. Guan, C. Burda and L. Guo, Metal Oxide-Based Tandem Cells for Self-Biased Photoelectrochemical Water Splitting, *ACS Energy Lett.*, 2020, **5**, 844–866, DOI: 10.1021/acsenergylett.9b02620.

100 C. Zhen, R. Chen, L. Wang, G. Liu and H. M. Cheng, Tantalum (oxy)nitride based photoanodes for solar-driven water oxidation, *J. Mater. Chem. A*, 2016, **4**, 2783–2800, DOI: 10.1039/c5ta07057k.

101 P. Y. Hsieh, J. Y. Wu, T. F. M. Chang, C. Y. Chen, M. Sone and Y. J. Hsu, Near infrared-driven photoelectrochemical water splitting: review and future prospects, *Arabian J. Chem.*, 2020, DOI: 10.1016/j.arabjc.2020.05.025.

102 Y. H. Chiu, K. D. Chang and Y. J. Hsu, Plasmon-mediated charge dynamics and photoactivity enhancement for Au-decorated ZnO nanocrystals, *J. Mater. Chem. A*, 2018, **6**(10), 4286–4296.

103 Y. H. Chiu, T. H. Lai, M. Y. Kuo, P. Y. Hsieh and Y. J. Hsu, Photoelectrochemical cells for solar hydrogen production: Challenges and opportunities, *APL Mater.*, 2019, **7**(8), 080901.